

DISCOVERY OF MOLECULAR SHELLS ASSOCIATED WITH SUPERNOVA REMNANTS. (I) KESTEEVEN 69

XIN ZHOU¹, YANG CHEN¹, YANG SU^{1,2}, JI YANG^{2,3}

¹ Department of Astronomy, Nanjing University, Nanjing 210093, P.R. China

² Purple Mountain Observatory, Chinese Academy of Sciences, Nanjing 210008

³ National Astronomical Observatories, Chinese Academy of Sciences, Beijing 100012

Draft version March 12, 2019

ABSTRACT

Supernova remnant (SNR) Kes 69 is morphologically characterized by the brightened radio, infrared, and X-ray emission on the southeastern rim, with the 1720 MHz OH masers detected in northeastern and southeastern regions at various LSR velocities. We have performed a millimeter observation in CO and HCO⁺ lines toward Kes 69. From the northeastern compact maser region, the ¹²CO and ¹³CO emission's peaks around 65 km s⁻¹ and 85 km s⁻¹ which are consistent with the masers' LSR velocities are detected. In the southeast, a molecular (¹²CO) arc is revealed at 77–86 km s⁻¹, well coincident with the partial SNR shell detected in the radio continuum and mid-infrared observations. An 85 km s⁻¹ HCO⁺ emission is found to arise from a radio peak on the shell. Both the molecular arc and the HCO⁺ emission at ~ 85 km s⁻¹ seem to be consistent with the presence of the extended OH masers along the southeastern boundary of Kes 69. The morphology correspondence between the CO arc and other band emission of the Kes 69 shell provides strong evidence for the association between SNR Kes 69 and the ~ 85 km s⁻¹ component of molecular gas. The multiwavelength emissions along the southeastern shell can be accounted for by the impact of the SNR shock on a dense, clumpy patch of molecular gas. This pre-existing gas is likely to be a part of the cooled debris of the material swept up by the progenitor's stellar wind. The association of SNR Kes 69 with the molecular cloud at the systemic velocity ~ 85 km s⁻¹ enables us to place the SNR at a kinematic distance of 5.2 kpc.

Subject headings: ISM: individual (Kes 69, G21.8–0.6) – ISM: molecules – supernova remnants

1. INTRODUCTION

The progenitors of core-collapse supernovae are most probably formed in giant molecular clouds (MCs). Due to the short lifetime, they are not far away from their matrices when they explode. Therefore it is common that the supernova remnants (SNRs) are located in the vicinity of MCs and may encounter them in evolution. The association with MCs often results in irregular morphology of the SNRs in multiwavelengths, which indicates sophisticated shock interaction with the inhomogeneous environmental medium. About twenty SNRs have been discovered to physically interact with ambient molecular gas based on the detection of the 1720 MHz OH masers (Frail et al. 1996), which are believed to be a tracer of the shock interaction with MCs (Lockett et al. 1999; Frail & Mitchell 1998; Wardle & Yusef-Zadeh 2002).

SNR Kesteven 69 is thought to probably be associated with MCs, because of the OH masers detected toward this remnant; however, the masers are found at various local standard rest (LSR) velocities and at various projected locations. Green et al. (1997) detected a compact OH maser by the Very Large Array (VLA) and the Australia Telescope Compact Array (ATCA) at $V_{\text{LSR}} = 69.3$ km s⁻¹ which is located projectionally in the northeastern part of the remnant. Recently Hewitt, Yusef-Zadeh, & Wardle (2008) not only found that this compact maser also has faint emission at 85 km s⁻¹, but also detected extended OH maser emission at the velocity ~ 85 km s⁻¹ with the Green Bank Telescope observation and the VLA archival observation toward the southern bright radio shell. The different LSR systemic velocities implies the MCs at different distances which may be im-

pacted by the SNR shock wave. Therefore investigation is needed to clarify at which systemic velocity the maser emission is the product of the Kes 69 shock interaction.

Kes 69 has an irregular X-ray morphology, as observed by *ROSAT* and *Einstein*, inside an incomplete radio shell (Seward 1990; Yusef-Zadeh et al. 2003). The *Spitzer* IRAC mid-infrared (IR) observation toward Kes 69 shows an arc at 4.5 μ m in the same location as the southeastern radio shell (Reach et al. 2006). The extended OH emission along the southern incomplete radio and IR shell hints an interaction of the SNR with the dense molecular gas in the south. If the SNR/MC association is established, a big progress can be made toward resolving the open question of the disparate velocity maser components and the distance to Kes 69 can also be determined.

Motivated by the supposed association of Kes 69 with molecular gas, we have performed millimeter CO and HCO⁺ observations toward this remnant. The observations and results are described in §2 and §3, and the conclusion is summarized in §4.

2. OBSERVATION AND DATA REDUCTION

The observations of millimeter molecular emissions toward SNR Kes 69 were made in two epochs during 2006 November–2007 January and 2007 October–November with the 13.7-meter millimeter-wavelength telescope of the Purple Mountain Observatory at Delingha (hereafter PMOD). An SIS receiver was used to simultaneously observe the ¹²CO (J=1-0), ¹³CO (J=1-0), and C¹⁸O (J=1-0) lines. We mapped a 25' \times 25' area that contains the full extent of SNR Kes 69 via raster-scan mapping with the grid spacing of 30''–60''. The main-beam efficiency in the

observing epoch was 67% and the elevation calibration

was performed. The typical system temperature was around 140–280 K. Three Acousto-Optical spectrometer (AOS) were used as back end, and the corresponding spectral coverages were 145 MHz for ^{12}CO ($J=1-0$) and 43 MHz for both ^{13}CO ($J=1-0$) and C^{18}O ($J=1-0$), all divided into 1024 channels. The observed velocity ranges were -120 – $+260$ km s^{-1} for ^{12}CO , 11 – 127 km s^{-1} for ^{13}CO ($J=1-0$), and 10 – 128 km s^{-1} for C^{18}O ($J=1-0$). We also chose two points for the HCO^+ ($J=1-0$) line observation with long-time integration [122 minutes for point ($18^{\text{h}}32^{\text{m}}50^{\text{s}}$, $-10^{\circ}12'42''$) and 134 minutes for ($18^{\text{h}}33^{\text{m}}10^{\text{s}}$, $-10^{\circ}12'42''$)], with the velocity range -3 – $+141$ km s^{-1} . The baseline subtraction was performed with low-order polynomial fit. In Table 1 we list some observational parameters, such as the frequencies, the average rms noises of all final spectra, the channel separations, and the full width at half maximum (FWHM). All data were reduced using the GILDAS/CLASS package¹.

The HI line emission data of the archival VLA Galactic Plane Survey (VGPS) (Stil et al. 2006) were also processed. The observations were made by the Very Large Array (VLA) and the Green Bank Telescope, presented with the beam-size of $1'$, the velocity resolution of 1.56 km s^{-1} , and the rms noise of 2 K per 0.824 km s^{-1} channel. The processed *Spitzer* Infrared Array Camera (IRAC; Fazio et al. 2004) Basic Calibrated Data were used here (PID: 146, PI: Ed Churchwell), which are available in the archive of the *Spitzer* Science Center and include flat-field correction, linearity and flux calibrations, and dark subtraction. The final mosaic $4.5\mu\text{m}$ IR image was produced by further processing with the custom IDL software (Huang et al. 2004). We also used the archived *Spitzer* Multiband Imaging Photometer (MIPS; Rieke et al. 2004) Post Basic Calibrated Data to present the mid-IR $24\mu\text{m}$ image, which were obtained from the Micron Survey of the Inner Galactic Disk Program (PID: 20597, PI: Sean Carey). The 1.4 GHz radio continuum emission data were obtained from the NRAO VLA Sky Survey (Condon et al. 1998).

3. RESULTS

3.1. The CO and HCO^+ Emissions

Figure 1 shows three CO spectra toward the center ($18^{\text{h}}32^{\text{m}}50^{\text{s}}$, $-10^{\circ}06'42''$) of the mapping area. There are several velocity components in the velocity range 0 – 120 km s^{-1} in the ^{12}CO ($J=1-0$) spectrum, and no ^{12}CO emission is detected out of this range in the whole mapping area. The ^{12}CO emission peaks appear in the intervals ~ 2 – 12 , 40 – 60 , 60 – 76 , 76 – 100 , and 107 – 120 km s^{-1} . We have found no morphological correspondence between the CO emission in the velocity intervals 2 – 12 km s^{-1} and 40 – 60 km s^{-1} and the emission from Kes 69 in any other waveband. The molecular component at around 110 km s^{-1} also shows no morphological correspondence, which is near the tangent point in this direction. Applying the rotation curve of Clemens (1985) together with

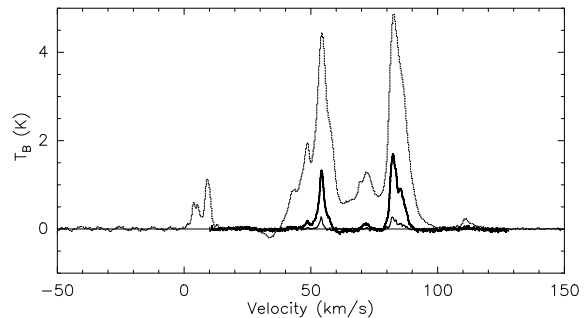


FIG. 1.— The spectra of the central point ($18^{\text{h}}32^{\text{m}}50^{\text{s}}$, $-10^{\circ}06'42''$) of the field of view in our observation toward Kes 69, dashed line for ^{12}CO , thick solid line for ^{13}CO , and thin solid line for C^{18}O . The signal-to-noise ratio is highest here. The small dip near 33 km s^{-1} results from the weak emission at the reference position, which is far from the concerned velocities.

$R_0 = 8.0$ kpc (Reid 1993) and $V_0 = 220$ km s^{-1} , the tangent point in this direction is at 7.4 kpc at 113.7 km s^{-1} . For the ^{12}CO emission, we focused our analysis on the velocity intervals 60 – 76 and 76 – 100 km s^{-1} , which respectively cover 69.3 km s^{-1} and 85 km s^{-1} at which the OH masers were detected. The ^{13}CO ($J=1-0$) emission is prominent at around 54 km s^{-1} and 82 km s^{-1} , at which ^{12}CO emission is strong. The intensity of C^{18}O ($J=1-0$) emission is too weak to examine its spatial distribution.

We have produced ^{12}CO intensity maps with interval 1 km s^{-1} between 60 and 76 km s^{-1} (Fig. 2) to examine the molecular gas around 69.3 km s^{-1} , at which the compact OH maser is seen. In the northeastern compact maser region, some faint diffuse ^{12}CO emission at 60 – 70 km s^{-1} are present. A distinct cloud at 69 – 76 km s^{-1} is seen in the west.

We have also produced ^{12}CO intensity maps over the velocity range of 76 – 92 km s^{-1} with interval 1 km s^{-1} (Fig. 3). By comparison with the radio continuum emission, an arc of the molecular gas at 77 – 86 km s^{-1} is strikingly coincident along the southeastern rim. This arc is clearly seen in the close-up intensity images at 80 – 81 km s^{-1} (Fig. 4) and 79 – 82 km s^{-1} (Fig. 5). In the northwest (see Figs. 4 and 5), there is another section of molecular arc, which can even be discerned in the wider range 79 – 86 km s^{-1} (Fig. 3). The two sections of molecular arcs are seen in similar velocity range and can be threaded with a circle of angular radius $8.7'$. Some bright, complicated ^{12}CO features are present in the field of view at 80 – 88 km s^{-1} . There may be a contribution from the HII region G21.902– 0.368 in the northwest, where the recombination line at 79.5 km s^{-1} has been detected (Lockman 1989). There is also a molecular cloudlet at 87 – 91 km s^{-1} , coincident with the strongest southern radio peak, at the western end of the incomplete radio shell. If this small cloud is associated with the SNR, the radio peak can be accounted for by the impact of the remnant shock on it, because of the drastic shock deceleration and hence the magnetic field compression and amplification.

¹ <http://www.iram.fr/IRAMFR/GILDAS>

TABLE 1
OBSERVATIONAL PARAMETERS

Line	frequency (GHz)	noise ^a (K)	Δv^b (km s ⁻¹)	FWHM (")
¹² CO (J=1-0)	115.271204	0.29	0.37	60
¹³ CO (J=1-0)	110.201353	0.24	0.11	60
C ¹⁸ O (J=1-0)	109.782183	0.20	0.12	60
HCO ⁺ (J=1-0)	89.188526	0.04	0.14	78

^a Average rms noise of all final spectra;

^b Channel separation.

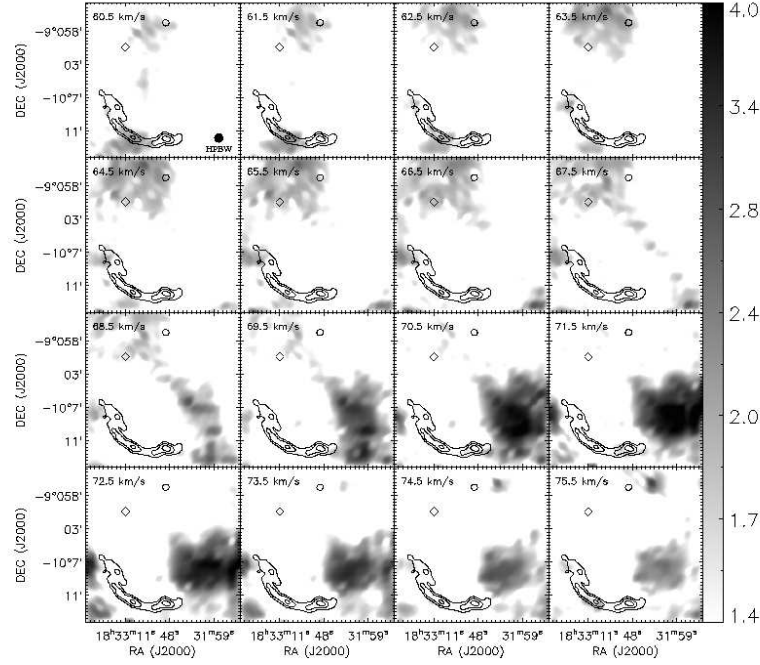


FIG. 2.— ¹²CO J=1-0 emission maps integrated each 1 km s⁻¹ (smoothed to an angular resolution of 0.4' by linear interpolation), with the NVSS 1.4 GHz radio continuum emission in contours (contour levels are 20, 49 and 107 mJy/beam). Central velocities are indicated in each image. The rms noise of each map is ~ 0.18 K km s⁻¹ and the beam size is 1'. The diamond denotes the location of the compact maser at 69.5 km s⁻¹.

The CO spectra from the northeastern compact OH maser region and the southeastern shell region are shown in Figure 6 (the two regions for CO spectrum extraction are shown in Figure 4). For the former region, the ¹²CO and ¹³CO emission peak at both ~ 65 and 85 km s⁻¹ (both with signal-to-noise ratio $S/N > 3$), essentially in agreement with the velocities at which the single maser arises (Green et al. 1997; Hewitt et al. 2008). The ¹²CO and ¹³CO lines at ~ 65 km s⁻¹ have complicated profiles, each of which can be phenomenologically fitted with a combination of at least three Gaussians. The lines at 85 km s⁻¹ are slightly broadened in the blue wings. For the latter region, there are ¹²CO and ¹³CO lines at 85 km s⁻¹, with blue wings broadened (although the wing

may be contaminated by the 72 km s⁻¹ peaks). The profile of each line is divided into a Gaussian at 85 km s⁻¹ and a residual part in the blue wing, with the fitted and derived parameters summarized in Table 2.

In the derivation, we used two methods to estimate the H₂ column density and molecular mass. In the first method, the H₂ column density is estimated by use of the conversion factor $N(\text{H}_2)/W(^{12}\text{CO}) \approx 1.8 \times 10^{20} \text{ cm}^{-2} \text{ K}^{-1} \text{ km}^{-1} \text{ s}$ (Dame et al. 2001). In the second method, we assume local thermodynamical equilibrium (LTE) for the gas and optically thick condition for the ¹²CO (J=1-0) line and use the relation $N(\text{H}_2) \approx 7 \times 10^5 N(^{13}\text{CO})$ (Frerking et al. 1982).

There seems to be a weak feature at 82 km s⁻¹ in the ¹³CO line profile of the southeastern region, which could be either a broadened part of the 85 km s⁻¹ component or a chance coincidence of an irrelevant, unperturbed cloud

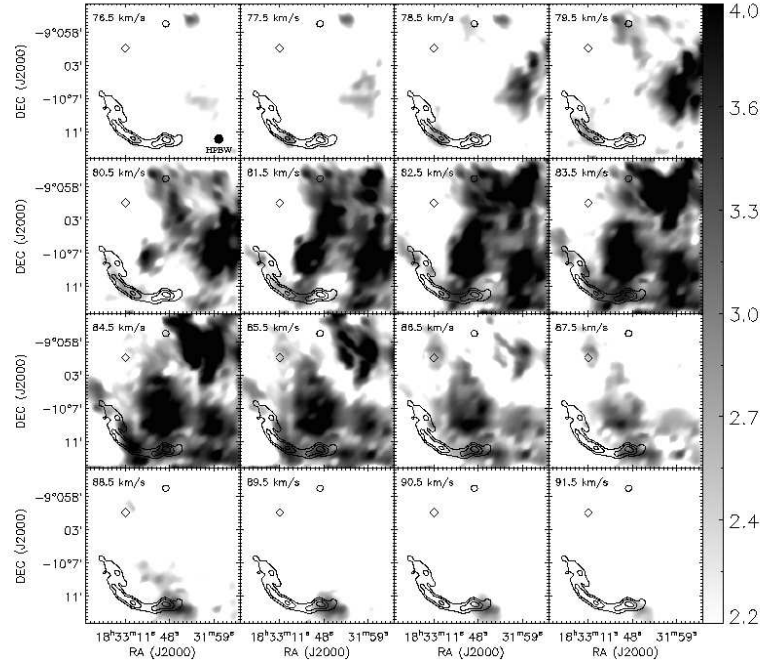


FIG. 3.— The same as for Figure 2, but the different velocity.

TABLE 2
FITTED AND DERIVED PARAMETERS FOR THE MCS AROUND 85 km s^{-1} IN THE SOUTHEASTERN REGION^a

Line	Gaussian Components		T_{peak} (K)	W (K km s^{-1})
	Center (km s^{-1})	FWHM (km s^{-1})		
^{12}CO (J=1-0)	84.7	5.2	2.4	13.4
^{13}CO (J=1-0)	84.9	2.4	0.5	1.2
Molecular Gas Parameters				
	$N(\text{H}_2)$ (10^{21} cm^{-2}) ^b	$M(M_{\odot})$ ^b	T_{ex} (K) ^c	$\tau(^{13}\text{CO})$ ^d
Gaussian components:	2.4 / 1.6	$5.8 \times 10^3 d_{5.2}^2 / 3.8 \times 10^3 d_{5.2}^2$ ^e	7.8	0.2
Residual part ^f :	2.2	$5.2 \times 10^3 d_{5.2}^2$ ^e		
The whole ^g :	4.6	$1.1 \times 10^4 d_{5.2}^2$ ^e		

^a The region is defined in Figure 4.^b See text for the two estimating methods.^c The excitation temperature calculated from the maximum ^{12}CO (J=1-0) emission point in the region.^d The optical depth of the ^{13}CO (J=1-0) line.^e $d_{5.2} = d/(5.2 \text{ kpc})$ (see §3.3).^f Determined by subtracting the Gaussian components centered at 72 km s^{-1} and 85 km s^{-1} after the multiple Gaussian fitting for the ^{12}CO (J=1-0) emission in the velocity range $70\text{--}95 \text{ km s}^{-1}$.^g Combination of the Gaussian components around 85 km s^{-1} and the residual part.

in the line of sight. We performed a multiple Gaussian fit incorporating this feature and derived a molecular gas mass for this feature, which is about two orders lower than the virial mass, indicating that the cloud is perturbed. In view of this and the clear shell-like appearance at $80\text{--}82 \text{ km s}^{-1}$, we treat it simply as a small part in the broaden wing of the 85 km s^{-1} gas.

In the long-time pointing observation toward the southern strongest radio peak or the cloudlet mentioned above, which targets at $(18^{\text{h}}32^{\text{m}}50^{\text{s}}.0, -10^{\circ}12'42'')$, no HCO^+ signal was detected. However, HCO^+ emission

was detected in the pointing observation toward another radio peak at $(18^{\text{h}}33^{\text{m}}10^{\text{s}}.0, -10^{\circ}12'42'')$ on the southeastern shell. The ^{12}CO , ^{13}CO , and HCO^+ spectra of this point are shown in Figure 7. The HCO^+ emission appears to only be prominent at $\sim 85 \text{ km s}^{-1}$, at which both the ^{12}CO and ^{13}CO emission peak, too. We calculated the column density of HCO^+ assuming that the HCO^+ emission is in LTE with the same excitation temperature as the ^{12}CO emission ($\sim 7.8 \text{ K}$) and is optically thin. For comparison with the CO column density, we smoothed the CO (J=1-0) data to the same angu-

TABLE 3
FITTED AND DERIVED PARAMETERS FOR THE HCO^+ EMITTING POINT ($18^{\text{h}}33^{\text{m}}10^{\text{s}}.0$, $-10^{\circ}12'42''$)

Line	Gaussian Components		T_{peak} (K)	W (K km s $^{-1}$)
	Center (km s $^{-1}$)	FWHM (km s $^{-1}$)		
^{12}CO (J=1-0)	85.0	3.4	3.9	14.3
^{13}CO (J=1-0)	84.9	2.4	0.5	1.2
HCO^+ (J=1-0)	85.0	2.2	0.2	0.5
Molecular Gas Parameters				
$N(^{13}\text{CO})$ (10^{15} cm $^{-2}$)	$N(\text{HCO}^+)$ (10^{11} cm $^{-2}$)	$\tau(^{13}\text{CO})$		
1.3	3.5	0.13		

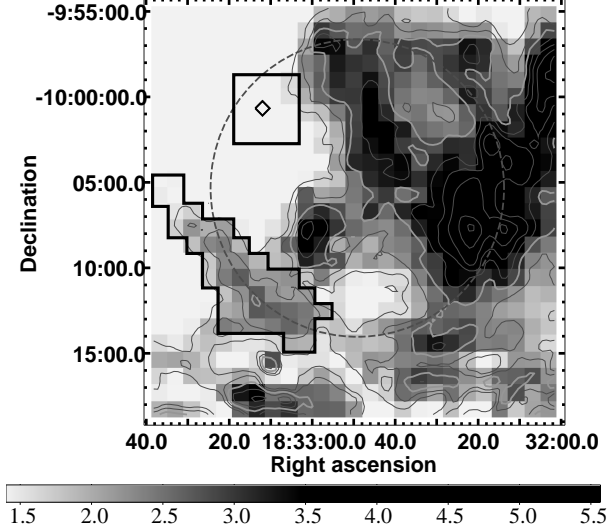


FIG. 4.— ^{12}CO (J=1-0) intensity map in the velocity interval 80–81 km s $^{-1}$. The intensity contours (smoothed to a resolution of $0.24'$ by interpolation) are at linear scale levels from 1.67 to 5.57 K km s $^{-1}$ in step of 0.6 K km s $^{-1}$, and the thick contour denotes the half-maximum intensity (2.79 K km s $^{-1}$). The rms noise is ~ 0.18 K km s $^{-1}$. The dashed circle is plotted roughly running through the molecular arcs in the southeast and the northwest, with an angular radius $8.7'$. The diamond denotes the location of the compact OH maser at 69.3 km s $^{-1}$. Two regions for CO spectrum extraction which overlap the northeastern OH maser and southeastern CO arc are also shown.

lar resolution as the HCO^+ observation, and the results are listed in Table 3. Considering the $^{12}\text{CO}/^{13}\text{CO}$ ratio (30–70) of the general interstellar medium (Langer 1992 and references therein), the HCO^+/CO abundance ratio is $\sim 5 \times 10^{-6}$. It is somewhat less than that of undisturbed cold MCs such as TMC-1 or L134N (1×10^{-4} ; Ohishi, Irvine, & Kaifu 1992). The HCO^+ abundance is expected to be reduced in a slow, nondissociating shock, unless some enhanced ionization is present (Iglesias & Silk 1978; Elitzur 1983). We note that the extended maser emission on the southern rim is found at the same LSR velocity (Hewitt et al. 2008), which implies that the dense molecular gas at this velocity is disturbed by C-type shock. For the origin of HCO^+ emission, though, further observation is needed to make a decision.

3.2. Morphological correlation in multiwavelengths

Combination of the multiwavelength observations toward Kes 69 (Fig. 5) shows some interesting morphological correlation.

First, the southeastern 77–86 km s $^{-1}$ molecular shell is not only coincident well with the 1.4 GHz radio shell (as

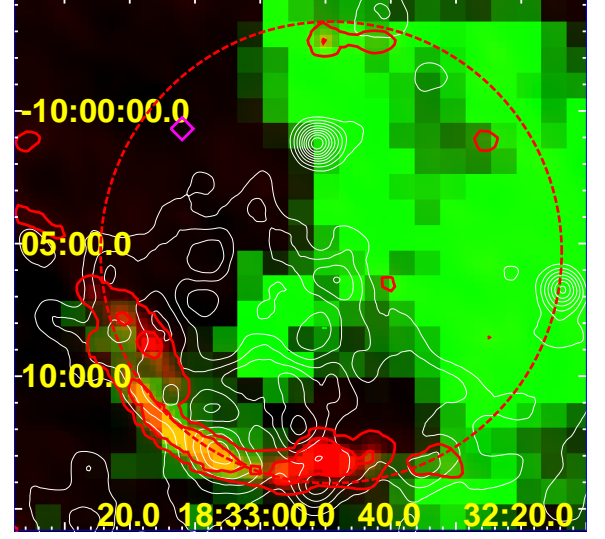


FIG. 5.— ^{12}CO (J=1-0) intensity map in the velocity interval 79–82 km s $^{-1}$ (above 5σ) coded in green, overlaid with the ROSAT PSPC X-ray contours in white and the NVSS radio continuum emission in red (the contour levels are 10, 41, and 172 mJy/beam). The diamond denotes the location of the compact OH maser at 69.3 km s $^{-1}$. The dashed circle is plotted roughly running through the molecular arcs in the southeast and the northwest, with an angular radius $8.7'$.

pointed out above), but also (as seen in Fig. 8) with the mid-IR “ridge” described in Reach et al. (2006). This mid-IR ridge is prominent in $4.5\mu\text{m}$, with a relatively high brightness in $5.8\mu\text{m}$. A part of the $24\mu\text{m}$ floc-like emission in the southeast is also aligned with the molecular shell (Fig. 8). The presence of the molecular shell is consistent with the HCO^+ and extended 1720 MHz OH maser emission at 85 km s $^{-1}$ along the southern rim. This correspondence in morphological features is most probably another signature of the SNR-MC interaction, in addition to the 1720 MHz OH masers detected to Kes 69.

Secondly, as described above, the both sections of molecular arcs at ~ 77 –86 km s $^{-1}$ in the southeast and the northwest seem to be aligned along a circle. A faint 1.4 GHz bar in the north (highlighted by a red contour in Fig. 5) is also along this circle. Moreover, as noted by Yusef-Zadeh et al. (2003), there is a faint radio shell in the northwest in the low-resolution 330 MHz image of Kes 69 (Kassim 1992), which is confused with the HII region G21.902–0.368. We note that the peak of this patch of radio emission roughly coincides with the northwestern section of molecular arc.

These morphological correlations demonstrate that Kes 69 is associated with the giant MC at the systemic

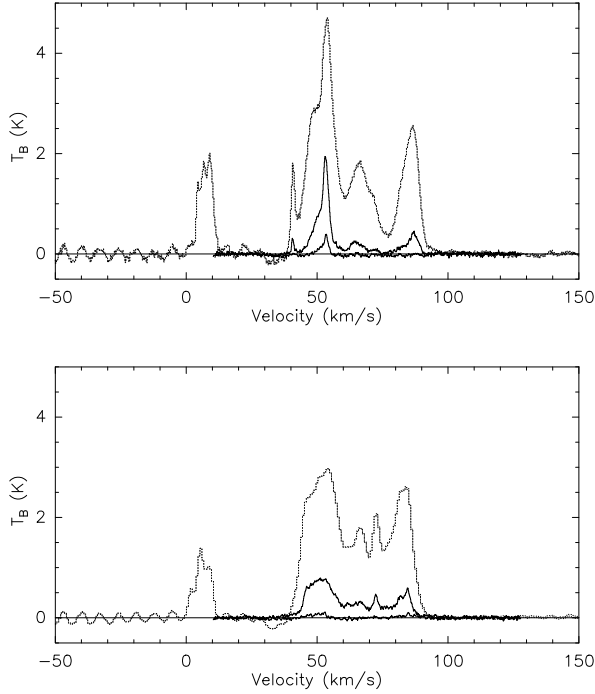


FIG. 6.— The CO spectra from the two regions that are defined in Figure 4. The upper panel is for the northeastern region covering the compact maser and the lower panel for the southeastern shell region. The dashed lines stand for the ^{12}CO emission, the thick solid lines for ^{13}CO , and the thin solid lines for C^{18}O . The sinusoidal pattern above the noise limit that appears in the ^{12}CO spectra for negative LSR velocities originates from the nonlinear response of the AOS system.

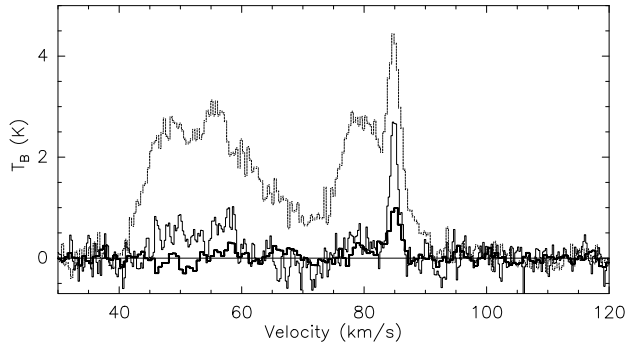


FIG. 7.— The spectra of the point ($18^{\text{h}}33^{\text{m}}10^{\text{s}}.0$, $-10^{\circ}12'42''$) on the southeastern rim of Kes 69, dashed line for ^{12}CO , thin solid line for two times the intensity of ^{13}CO , and thick solid line for five times the intensity of HCO^+ . The noise level for the HCO^+ emission is given in Table 1, together with those for the CO lines.

velocity $\sim 85 \text{ km s}^{-1}$. This association is strengthened by the detection of the extended and compact 1720 MHz OH maser emission and the HCO^+ emission at 85 km s^{-1} from the SNR region.

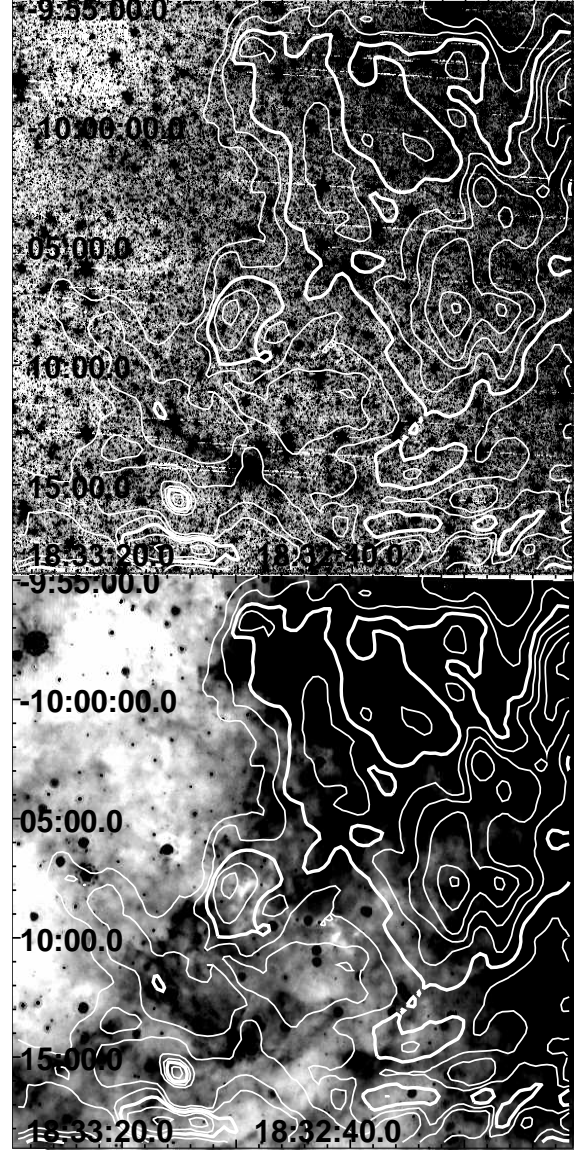


FIG. 8.— *Spitzer* $4.5\mu\text{m}$ (upper panel) and $24\mu\text{m}$ (bottom panel) greyscale images overlaid with the $80\text{--}81 \text{ km s}^{-1}$ ^{12}CO ($J=1-0$) intensity contours (the same as in Fig. 4).

The southeastern half of the circle is roughly X-ray bright, while the other half appears to be X-ray faint but covered by the $79\text{--}82 \text{ km s}^{-1}$ molecular gas. This brightness anticorrelation between the X-ray and CO emission, however, does not imply that the molecular gas in the northwestern half obscures the X-rays. We estimate the hydrogen column density of this gas (in the interval $79\text{--}82 \text{ km s}^{-1}$) to be $N_H \sim 1 \times 10^{21} \text{ cm}^{-2}$. If there were an X-ray emitting gas, with similar properties to that observed in the southeast (temperature $kT_x \sim 1.6 \text{ keV}$ and intervening hydrogen column $2.4 \times 10^{22} \text{ cm}^{-2}$; Yusef-Zadeh et al. 2003), behind this northwestern molecular gas, then an extra extinction by the $N_H \sim 1 \times 10^{21} \text{ cm}^{-2}$ gas would only cause a $\sim 8\%$ decrease in the $0.5\text{--}2 \text{ keV}$ X-ray flux and this X-ray emission could have been observable. Thus we conclude that the X-ray faintness in the northwest is not caused by the absorption of the diffuse $79\text{--}82 \text{ km s}^{-1}$ molecular gas, no matter whether this gas is connected to the $\sim 85 \text{ km s}^{-1}$ cloud or not.

3.3. The Dynamics

The association between SNR Kes 69 and the MC at systemic velocity 85 km s^{-1} facilitates a convincing determination of the kinematic distance to the remnant. The systemic velocity 85 km s^{-1} is suggestive of two candidate kinematic distances to the SNR/MC association, 5.2 kpc and 9.6 kpc. The choice can be made with the aid of the HI absorption along the line of sight. Following the method used in Tian, Leahy, & Wang (2007) and Tian & Leahy (2008a), we produced three HI spectra of regions along the southeastern shell of Kes 69, as shown in Figure 9. Distinct absorption features appear at 4, 6, 15, 40, 48, 67, 70, 82, and 88 km s^{-1} . The ^{12}CO components along the shell around 5 and 50 km s^{-1} (Fig. 6) can, due to the corresponding absorption features in the HI spectra, be related to the chance-coincident foreground gas. No HI absorption features are present around the tangent point velocity 113.7 km s^{-1} , which indicates that the SNR is in front of the tangent point (at 7.4 kpc). Hence, the distance to the SNR is $d = 5.2 \text{ kpc}$. We note that a similar estimate is meantime given by Tian & Leahy (2008b).

The southeastern molecular arc is revealed above to be coincident with the radio and IR shell and move at a velocity v_m of order 10 km s^{-1} (matching the blueshifted line broadening which reflects the velocity component in the line of sight). The broadened blue wing of the $\sim 85 \text{ km s}^{-1}$ line profile of the molecular arc implies that the giant molecular cloud may have suffered a perturbation from the rear side. Three scenarios regarding the dynamical relation between the molecular arc and the SNR are discussed below.

Firstly, the arc is likely to be a flake of molecular gas that is shocked by the slow transmitted cloud shock after the SNR blast wave hits the molecular cloud. In this case, the radio continuum emission may arise from the SNR shock that is blocked by dense cloud (Frail & Mitchell 1998) or the blast wave that propagates in the intercloud medium (Blandford & Cowie 1982), and the thermal X-ray emission may be ascribed to the hot gas behind the shocked molecular gas or just behind the blast wave. Thus there can be a crude pressure balance between the cloud shock and the X-ray emitting hot gas (Zel'dovich & Raizer 1967; McKee & Cowie 1975): $n_0 v_b^2 \sim n_m v_m^2$, where n_m denotes the number density of the hydrogen atoms ahead of the cloud shock, n_0 the density of the undisturbed intercloud medium, and v_b the velocity of the blast wave. Velocity v_b is related to the postshock temperature kT_x as $v_b = [16kT_x/(3\bar{\mu}m_H)]^{1/2}$, where m_H is the hydrogen atom mass and $\bar{\mu} = 0.61$ is the average atomic weight. Adopting $kT_x \sim 1.6 \text{ keV}$ from the *ROSAT* X-ray observation (Yusef-Zadeh et al. 2003), we have $v_b \sim 1.2 \times 10^3 \text{ km s}^{-1}$ and $n_m \sim 1.3 \times 10^3 (n_0/0.1 \text{ cm}^{-3})(v_m/10 \text{ km s}^{-1})^{-2} \text{ cm}^{-3}$, implying that the blast wave hits a very dense matter in the molecular arc (here n_0 is assumed to be similar to the mean density of the X-ray emitting gas, $\sim 0.1 \text{ cm}^{-3}$, as obtained from a reproduced *ROSAT* X-ray spectral analysis²). In this scenario, assuming an adiabatic expansion and adopting the SNR extent represented by the

circle of radius $\sim 8.7'$ ($\S 3.2$) or $r_s \sim 13d_{5.2} \text{ pc}$, the SNR's age is estimated as $t = (2r_s)/(5v_b) \sim 4.4d_{5.2} \text{ kyr}$ and the explosion energy is $E = (25/4\xi)(1.4n_0m_H)v_b^2r_s^3 \sim 6 \times 10^{50} (n_0/0.1 \text{ cm}^{-3})d_{5.2}^3 \text{ ergs}$ (where $\xi = 2.026$).

The $4.5\mu\text{m}$ and $5.8\mu\text{m}$ mid-IR emissions are suggested to be likely dominated by lines of shocked gas (Reach et al. 2006). They note that the $5.8\mu\text{m}$ emission is relatively strong, but it is not clear whether H_2 or $[\text{Fe II}]$ lines (as likely mechanisms) are responsible for this emission, unlike the case of IC 443, in which the $[\text{Fe II}]$ and H_2 lines are very clearly segregated to the northern and southern regions of the remnant, respectively (see Rho et al. 2001). The H_2 emission seems to be consistent with the slow molecular shock, while $[\text{Fe II}]$ emission could not be ruled out with the present observations if the SNR shocks propagate in a complicated multi-phase medium. The $24\mu\text{m}$ emission along the arc is likely to arise from the shocked molecular gas (e.g., OH and H_2O), shock-heated dust grains, and even probably ions. The OH maser, HCO^+ , and H_2O (if any) emission are consistent with a C-type molecular shock.

Secondly, let us discuss the scenario in which the arc represents the interstellar material swept up all the way by the SNR shock wave. The mass of the southeastern molecular arc is in the range of $0.5\text{--}1.1 \times 10^4 d_{5.2}^2 M_\odot$, with the gas mass observed in the whole line profile adopted as the upper limit and that of the broadened part as the lower limit (Table 2). In the swept-up case, the southeastern arc consists of the molecular gas which was originally of mean density $n(\text{H}_2) \sim 30\text{--}70 d_{5.2}^{-1} \text{ cm}^{-3}$, distributed in an approximate $1/8$ volume of sphere of radius $r_s \sim 8.7' \sim 13d_{5.2} \text{ pc}$ (considering the one-sided line broadening). In this scenario, the velocity of the SNR shock is represented by the arc's slow expansion ($v_m \sim 10 \text{ km s}^{-1}$), which would imply that the SNR is in the radiative phase. The explosion energy of the SNR, $E \sim 7 \times 10^{50} (r_s/13 \text{ pc})^{3.12} [n(\text{H}_2)/50 \text{ cm}^{-3}]^{1.12} (v_m/10 \text{ km s}^{-1})^{1.4} \text{ ergs}$ (Chevalier 1974), would have seemed to be normal, despite the seldom large age $t \sim 0.31r_s/v_m \sim 4 \times 10^5 (r_s/13 \text{ pc})(v_m/10 \text{ km s}^{-1})^{-1} \text{ yr}$ for X-ray-bright SNRs. However, the X-rays are bright along the southern shell and two X-ray emission peaks are essentially coincident with the two radio peaks (Fig. 5) (toward which the pointing molecular line observation was made). A radiative shock as slow as 10 km s^{-1} could not be responsible for such X-rays along the SNR rim. On the other hand, to accelerate particles to relativistic energies for emitting radio synchrotron, the lower limit of the shock velocity is (Draine & McKee 1993): $v_s > 64(x_i/10^{-5})^{1/8} [n(\text{H}_2)/50 \text{ cm}^{-3}]^{1/8} (\phi_{\text{cr}}/0.1)^{-1/4} (T/100 \text{ K})^{0.1} \text{ km s}^{-1}$, where x_i is the ionization fraction, ϕ_{cr} the efficiency of the particle acceleration of the shock, and T the preshock molecular gas temperature. It is much larger than the observed expansion velocity of the molecular shell, and thus new particle acceleration would be difficult to take place at this shock. The existing relativistic electrons would rapidly stream freely away from the shock front for a very low ionization fraction (Blandford & Cowie 1982). More-

the volume emission measure $n_e n_H V \sim 7.9 \times 10^{57} d_{5.2}^2 \text{ cm}^{-3}$ of an elliptical region (with half-axes $11.2' \times 6.7'$), for which a volume of an oblate spheroid (with half-axes $11.2' \times 11.2' \times 6.7'$) is assumed.

² The mean density of the X-ray emitting gas is estimated as $\sim 0.14d_{5.2}^{-1/2} \text{ cm}^{-3}$ (where $d_{5.2} = d/5.2 \text{ kpc}$ is used for scaling) from

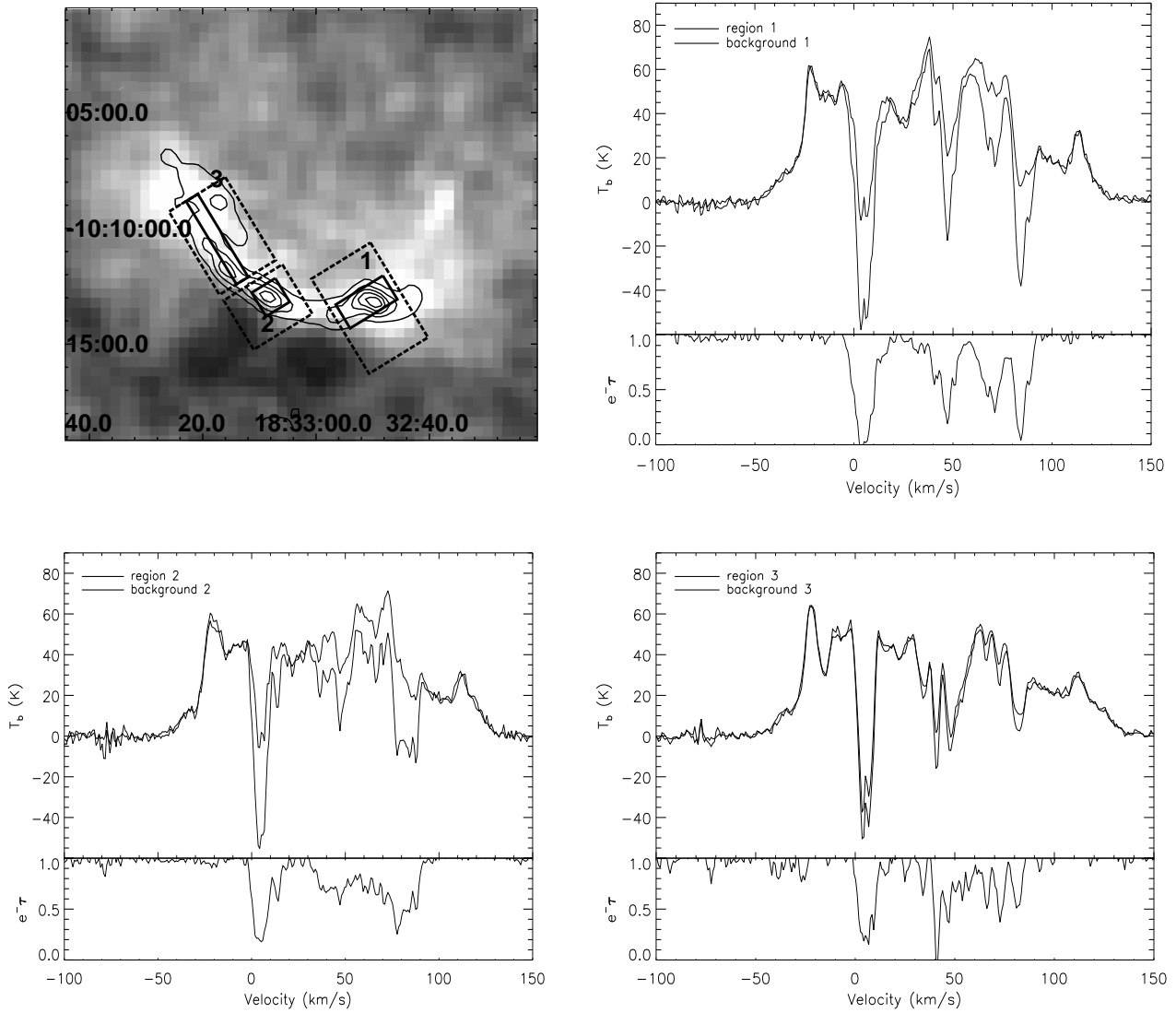


FIG. 9.— *Left-top panel:* HI emission map of Kes 69 from a single channel at 74.39 km s^{-1} , overlaid with NVSS radio continuum contours (with levels at 20, 49, 78, 107, 136 and 165 mJy/beam). The three pairs of regions are defined to extract the HI spectra. *Other three panels:* The source and background HI emission spectra and the absorption spectra extracted from the defined regions 1, 2 and 3, respectively.

over, because of the ambipolar diffusion, the magnetic field will separate from the neutral gas in a timescale (Blandford & Cowie 1982): $\sim 10^3 (\delta r / 1 \text{ pc})^2 (x_i / 10^{-5}) [n(\text{H}_2) / 50 \text{ cm}^{-3}]^2 (B / 10^{-6} \text{ G})^{-2} (s / 100)^{-2} \text{ yr}$ (where B is the magnetic field strength in the unshocked gas, s the density compression ratio, and δr the shell thickness), very likely to be smaller than the remnant age in this case (even for $s \sim 10$). Therefore, such a slow expansion of molecular cloud is difficult to account for the SNR's radio emission. In view of the above points, this scenario does not apply to the molecular shell of Kes 69.

Thirdly, the molecular shell may be the debris of the cooled, condensed material, which was swept up by the stellar wind of the supernova progenitor from the molecular gas [$n(\text{H}_2) \sim 50 \text{ cm}^{-3}$] and is now hit by the SNR shock. This possibility could be compatible with the first scenario and naturally explain why there is the pre-existing very dense material that is now hit by the SNR shock. A molecular wind-bubble shell has

recently been discovered coincident with the ring nebula G79.29+0.46 surrounding a luminous blue variable star (Rizzo et al. 2008), which provides an instance for this scenario. If there was a stellar-wind bubble, it was created (Castor et al. 1975; Weaver et al. 1977) $\sim 1.4 \times 10^6 (r / 13 \text{ pc})^{5/3} L_{36}^{-1/3} [n(\text{H}_2) / 50 \text{ cm}^{-3}]^{1/3} \text{ yr}$ ago, where L_{36} is the mechanical luminosity of the stellar wind in units of $10^{36} \text{ ergs s}^{-1}$, and the present velocity of the shell is $\sim 6 (r / 13 \text{ pc})^{-2/3} L_{36}^{1/3} [n(\text{H}_2) / 50 \text{ cm}^{-3}]^{-1/3} \text{ km s}^{-1}$. This velocity is comparable to the blueshift in the broadened line profile of the molecular gas along the shell.

There appears to be a blowout morphology outlined by the extension of the radio/CO shell to the northeast out of the circle (Figs. 4 and 5), somewhat similar to the blowout morphology in SNR N132D (e.g., Dickel & Milne 1995; Xiao & Chen 2008). Actually, SNR N132D, which is in the vicinity of a MC, has been suggested to be shaped by the shock impacting on the stellar wind-bubble

shell (Hughes 1987; Chen et al. 2003). The northeastern compact masers at both 69 and 85 km s^{-1} are projected in the blowout region. In this case, as a possibility, the 69 km s^{-1} maser could arise from a dense clump deviating from the systemic velocity by a strong perturbation, although it cannot be excluded from being non-associated with the same SNR.

4. SUMMARY

We have performed a millimeter observation in CO and HCO^+ lines toward SNR Kes 69. From the northeastern compact 1720 MHz OH maser region, the ^{12}CO and ^{13}CO emission's peaks around 65 km s^{-1} and 85 km s^{-1} which are consistent with the masers' LSR velocities are detected. In the southeast, a molecular ($^{12}\text{CO J}=1-0$) arc is revealed at $77-86 \text{ km s}^{-1}$, well coincident with the partial SNR shell detected in the 1.4 GHz radio continuum and mid-IR observations. An 85 km s^{-1} HCO^+ emission is found to arise from a radio peak on the shell. Both the molecular arc and the HCO^+ emission at $\sim 85 \text{ km s}^{-1}$ seems to be consistent with the presence of the extended 1720 MHz OH emission along the southeastern boundary of Kes 69. The morphology correspondence between the CO emission and other band emission of the Kes 69 shell provides strong evidence for the association of the

SNR with the $\sim 85 \text{ km s}^{-1}$ component of molecular gas. There is another section of molecular arc at $79-86 \text{ km s}^{-1}$ in the northwest. The both molecular arcs, together with the faint northern radio features, seem to be distributed along a circle of radius $8.7'$. The multiwavelength emissions along the southeastern shell can be explained by the impact of the SNR shock on a dense, clumpy patch of molecular gas. This pre-existing gas is likely to be a part of the cooled, clumpy debris of the interstellar molecular gas swept up by the progenitor's stellar wind. The association between SNR Kes 69 and the MC at the systemic velocity $\sim 85 \text{ km s}^{-1}$ enables us to place the SNR at a kinematic distance of 5.2 kpc.

We are grateful to the staff of Qinghai Radio Observing Station at Delingha for the support during the observation. We thank Wen-Wu Tian for advice on the distance estimates and other specific issues. Y.C. acknowledges support from NSFC grants 10725312, 10673003, and 10221001 and the 973 Program grant 2009CB824800. We acknowledge the use of the VGPS data; the National Radio Astronomy Observatory is a facility of the National Science Foundation operated under cooperative agreement by Associated Universities, Inc.

REFERENCES

- Blandford, R. D., & Cowie, L. L. 1982, *ApJ*, 260, 625
 Castor, J., McCray, R., & Weaver, R. 1975, *ApJ*, 200, L107
 Chen, Y., Zhang, F., Williams, R. M., & Wang, Q. D. 2003, *ApJ*, 595, 227
 Chevalier, R., A. 1974, *ApJ*, 188, 501
 Clemens, D. P. 1985, *ApJ*, 295, 422
 Condon, J. J., Cotton, W. D., Greisen, E. W., Yin, Q. F., Perley, R. A., Taylor, G. B., & Broderick, J. J. 1998, *AJ*, 115, 1693
 Dame, T. M., Hartmann, D., & Thaddeus, P. 2001, *ApJ*, 547, 792
 Draine, B. T. & McKee, C. F. 1993, *ARA&A*, 31, 373
 Dickel, J. R. & Milne, D. K. 1995, *AJ*, 109, 200
 Elitzur, M. 1983, *ApJ*, 267, 174
 Fazio, G. G., Hora, J. L., Allen, L. E., Ashby, M. L. N., Barmby, P., Deutsch, L. K., Huang, J.-S., Kleiner, S., Marengo, M., Megeath, S. T., Melnick, G. J., Pahre, M. A., Patten, B. M., Polizotti, J., Smith, H. A., Taylor, R. S., Wang, Z., Willner, S. P., Hoffmann, W. F., Pipher, J. L., Forrest, W. J., McMurty, C. W., McCreight, C. R., McKelvey, M. E., McMurray, R. E., Koch, D. G., Moseley, S. H., Arendt, R. G., Mentzell, J. E., Marx, C. T., Losch, P., Mayman, P., Eichhorn, W., Krebs, D., Jhabvala, M., Gezari, D. Y., Fixsen, D. J., Flores, J., Shakoordadeh, K., Jungo, R., Hakun, C., Workman, L., Karpati, G., Kichak, R., Whitley, R., Mann, S., Tollestrup, E. V., Eisenhardt, P., Stern, D., Gorjian, V., Bhattacharya, B., Carey, S., Nelson, B. O., Glaccum, W. J., Lacy, M., Lowrance, P. J., Laine, S., Reach, W. T., Stauffer, J. A., Surace, J. A., Wilson, G., Wright, E. L., Hoffman, A., Domingo, G., Cohen, M. 2004, *ApJS*, 154, 10
 Frail, D. A., Goss, W. M., Reynoso, E. M., Giacani, E. B., Green, A. J., & Otrupcek, R. 1996, *AJ*, 111, 1651
 Frail, D. A. & Mitchell, G. F. 1998, *ApJ*, 508, 690
 Frerking, M. A., Langer, W. D., & Wilson, R. W. 1982, *ApJ*, 262, 590
 Green, A. J., Frail, D. A., Goss, W. M., & Otrupcek, R. 1997, *AJ*, 114, 2058
 Hewitt, J. W., Yusef-Zadeh, F., & Wardle, M. 2008, *ApJ*, 683, 189
 Huang, J.-S., Barmby, P., Fazio, G. G., Willner, S. P., Wilson, G., Rigopoulou, D., Alonso-Herrero, A., Dole, H., Egami, E., Le Floch, E., Papovich, C., Prez-Gonzalez, P. G., Rigby, J., Engelbracht, C. W., Gordon, K., Hines, D., Rieke, M., Rieke, G. H., Meisenheimer, K., & Miyazaki, S. 2004, *ApJS*, 154, 44
 Hughes, J. P. 1987, *ApJ*, 314, 103
 Iglesias, E. R., & Silk, J. 1978, *ApJ*, 226, 851
 Kassim, N. 1992, *AJ*, 103, 943
 Langer, W. D. 1992, *IAUS*, 150, 193
 Lockman, F. J. 1989, *ApJS*, 71, 469
 Lockett, P., Gauthier, E., & Elitzur, M. 1999, *ApJ*, 511, L235
 McKee, C. F. & Cowie, L. L. 1975, *ApJ*, 195, 715
 Ohishi, M., Irvine, W. M., & Kaifu, N. 1992, *IAUS*, 150, 171
 Reach, W. T., Rho, J., Tappe, A., Pannuti, T. G., Brogan, C. L., Churchwell, E. B., Meade, M. R., Babler, B., Indebetouw, R., & Whitney, B. A. 2006, *AJ*, 131, 1479
 Reid, M. J. 1993, *ARA&A*, 31, 345
 Rieke, G. H., Young, E. T., Engelbracht, C. W., Kelly, D. M., Low, F. J., Haller, E. E., Beeman, J. W., Gordon, K. D., Stansberry, J. A., Misselt, K. A., Cadien, J., Morrison, J. E., Rivlis, G., Latter, W. B., Noriega-Crespo, A., Padgett, D. L., Stapelfeldt, K. R., Hines, D. C., Egami, E., Muzerolle, J., Alonso-Herrero, A., Blaylock, M., Dole, H., Hinz, J. L., Le Floch, E., Papovich, C., Perez-Gonzalez, P. G., Smith, P. S., Su, K. Y. L., Bennett, L., Frayer, D. T., Henderson, D., Lu, N., Masci, F., Pesenson, M., Rebull, L., Rho, J., Keene, J., Stolovy, S., Wachter, S., Wheaton, W., Werner, M. W., Richards, P. L. 2004, *ApJS*, 154, 25
 Rizzo, J. R., Jimenez-Esteban, F. M., & Ortiz, E. 2008, *ApJ*, 681, 355
 Rho, J., Jarrett, T. H., Cutri, R. M., & Reach, W. T. 2001, *ApJ*, 547, 885
 Seward, F. D. 1990, *ApJS*, 73, 781
 Stil, J. M., Taylor, A. R., Dickey, J. M., Kavars, D. W., Martin, P. G., Rothwell, T. A., Boothroyd, A. I., Lockman, F. J., & McClure-Griffiths, N. M. 2006, *AJ*, 132, 1158
 Tian, W. W., Leahy, D. A., & Wang, Q. D. 2007, *A&A*, 474, 541
 Tian, W. W. & Leahy, D. A. 2008a, *ApJ*, 677, 292
 ———, 2008b, *MNRAS*, in press
 Wardle, M. & Yusef-Zadeh, F., 2002, *Science*, 296, 2350
 Weaver, R., McCray, R., Castor, J., Shapiro, P., & Moore, R. 1977, *ApJ*, 218, 377
 Xiao, X. & Chen, Y. 2008, *AdSpR*, 41, 416
 Yusef-Zadeh, F., Wardle, M., Rho, J., & Sakano, M. 2003, *ApJ*, 585, 319
 Zel'dovich, Ya. B. & Raizer, Yu. M. 1967, *Physics of shock waves and high-temperature hydrodynamic phenomena* (New York: Academic Press)